Vibrational Coherence in Polar Solutions of Zn^{II} tetrakis(N-methylpyridyl)porphyrin with Soret-Band Excitation: Rapidly Damped Intermolecular Modes with Clustered Solvent Molecules and Slowly Damped Intramolecular Modes from the Porphyrin Macrocycle

Kevin L. Dillman, Katherine R. Shelly,[†] and Warren F. Beck*

Department of Chemistry, Michigan State University, East Lansing, Michigan 48824

Received: September 2, 2008; Revised Manuscript Received: December 24, 2008

Ground-state coherent wavepacket motions arising from intermolecular modes with clustered, first-shell solvent molecules were observed using the femtosecond dynamic absorption technique in polar solutions of Zn^{II} *meso*-tetrakis(N-methylpyridyl)porphyrin (ZnTMPyP) with excitation in the Soret absorption band. As was observed previously in bacteriochlorophyll *a* solution, the pump−probe transients in ZnTMPyP solutions are weakly modulated by slowly damped (effective damping time $\gamma > 1$ ps) features that are assigned to intramolecular modes, the skeletal normal modes of vibration of the porphyrin. The 40 cm^{-1} and 215 cm^{-1} modes from the metal-doming and metal−solvent-ligand modes, respectively, are members of this set of modulation components. A slowly damped 2−4 cm^{-1} component is assigned to the internal rotation of the N-methylpyridyl rings with respect to the porphyrin macrocycle; this mode obtains strong resonance Raman intensity enhancement from an extensive delocalization of π-electron density from the porphyrin in the ground state onto the rings in the π^* excited states. The dominant features observed in the pump−probe transients are a pair of rapidly damped ($\gamma < 250$ fs) modulation components arising from intermolecular modes with solvent molecules. This structural assignment is supported by an isotope-dependent shift of the average mode frequencies in methanol and perdeuterated methanol. The solvent dependence of the mean intermolecular mode frequency is consistent with a van der Waals intermolecular potential that has significant contributions only from the London dispersion and induction interactions; ion−dipole or ion−induced-dipole terms do not make large contributions because the π-electron density is not extensively delocalized onto the N-methylpyridyl rings. The modulation depth associated with the intermolecular modes exhibits a marked dependence on the electronic structure of the solvent that is probably related to the degree of covalency; the strongest modulations are observed in acetonitrile and dimethylsulfoxide. The results strongly support a structural assignment of the low-frequency modes that are coupled to the primary and secondary electron-transfer reactions in photosynthetic reaction centers to intermolecular modes between the redox-active chromophores and first-solvation shell groups from the surrounding protein, and an important additional function of the intermolecular modes in the stabilization of charged intermediates is suggested.

1. Introduction

In the purple-bacterial photosynthetic reaction center, the primary and secondary charge-separation reactions exhibit effectively activationless dynamics owing to coupling to low-frequency vibrational modes in the 100 cm^{-1} regime.[1−3] The main components detected in the vibrational coherence observed in pump−probe[4−12] and fluorescence upconversion[13] transients following impulsive excitation of the primary electron donor, *P*, are modes with frequencies in the 30−100 cm^{-1} range. The possibility that the modes observed in the vibrational coherence are the ones that are coupled to the electron-transfer reaction coordinate has been discussed,[10,14−20] but their structural origin remains indeterminate. Bixon and Jortner[1−3] attributed the coupled modes to the protein medium, and Vos, Martin, and co-workers suggested that the modes that are active in the vibrational coherence are delocalized or phonon-like in character.[6,11]

In recent work, we have advanced an alternative hypothesis that the vibrational modes that control the electron-transfer dynamics in reaction centers are intermolecular in origin, between the redox-active chromophores and the groups in the first-solvation shell from the surrounding protein medium. This hypothesis is supported by our observations using femtosecond pump−probe spectroscopy of the rapidly damped low-frequency vibrational coherence from bacteriochlorophyll *a* (BChl) in polar solution[21,22] and in the light-harvesting subunit proteins B777 and B820.[23] In solution, BChl exhibits a slowly damped set of modulations over the 100−8000 fs probe delay range; these components exhibit damping times in the >1 ps regime and mode frequencies ranging from 10 to 220 cm^{-1}. The magnitude spectrum obtained by Fourier transformation is comparable to the low-frequency region of the conventional resonance Raman spectrum from BChl in solution, in films, and in the reaction center,[24,25] so these slowly damped features are assigned to the low-frequency skeletal modes of the BChl macrocycle.[21] By far the strongest features in the vibrational coherence from BChl solutions, however, are a very rapidly damped set of modulation components in the subpicosecond time scale. These features are well-described by time-domain models that correspond in the frequency domain to inhomogeneously broadened lineshapes

* Corresponding author. E-mail: beck@msu.edu. Fax: 517-353-1793.
† Current address: Beckman Coulter, Inc., 100 Lake Hazeltine Blvd., Chaska, Minnesota 55318.
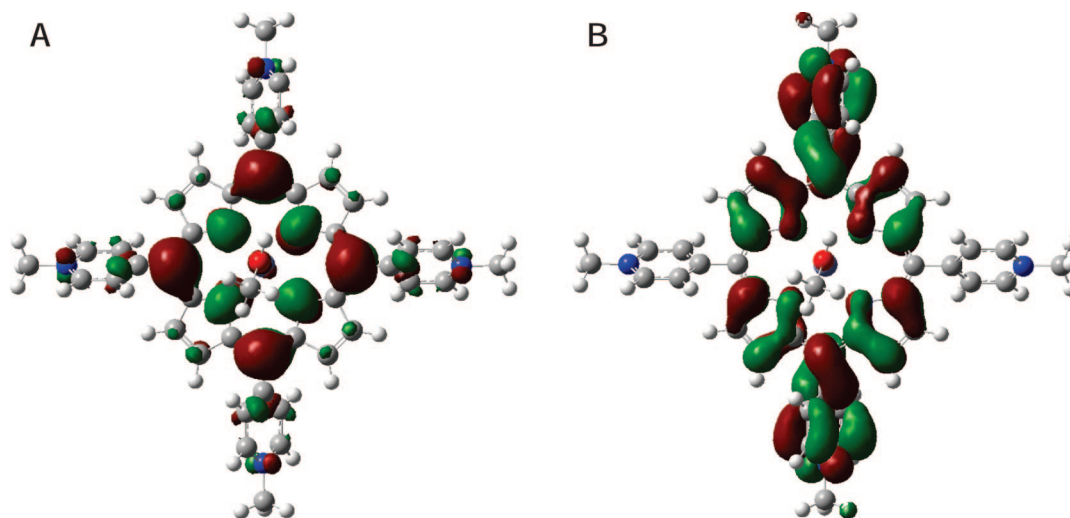
Figure 1. Optimized structure of Zn[II] *meso*-tetrakis(N-methylpyridyl)porphyrin (ZnTMPyP) complexed with a single methanol molecule as an axial ligand to the Zn[II] ion. The structure was obtained from a B3LYP hybrid density functional electronic structure calculation with Gaussian 03[32] at the 6−31G level of theory. The ball-and-stick structures are shown superimposed with density surfaces for (a) the highest occupied molecular orbital (HOMO) and for (b) the lowest unoccupied molecular orbital (LUMO).

with very broad, asymmetric Gaussian profiles. The mean frequency of the rapidly damped vibrational coherence exhibits a greater than quadratic dependence on the gas-phase dipole moment of the solvent. This trend is consistent with a van der Waals intermolecular potential in which the London-dispersion and dipole−dipole interactions make large contributions; the extrapolated 100 cm^{-1} frequency in the nonpolar limit arises predominantly from the London-dispersion term.[22] The rapidly damped vibrational coherence observed in the B777 system is comparable to that observed with BChl in acetone solution because the BChl macrocycles are exposed to the polar head groups of the surrounding nonionic detergent. In the paired BChl system called B820 that forms when two B777 monomers associate, however, the supporting α helices sterically protect the BChl macrocycles from direct attack by the surrounding detergent. The vibrational coherence then reveals weaker and more slowly damped components at 28 cm^{-1} and 46 cm^{-1} that are assigned to BChl−tryptophan and BChl−BChl intermolecular modes.[23]

The intermolecular modes that contribute to the vibrational coherence in BChl-containing systems modulate the pump−probe ground-state depletion signal owing to the resonant impulsive stimulated Raman scattering (RISRS) mechanism.[26−31] We suggest that these modes are resonance Raman active because molecules in the first solvation shell make a direct attack on the π-electron density above and below the macrocycle and are displaced by the π→π* transition.[22,23] This hypothesis suggests that the spatial organization of the π-electron density in the ground state selects the first-shell solvent molecules that contribute to the vibrational coherence. As a test of these ideas, we discuss in this contribution the low-frequency ground-state vibrational coherence in polar solutions of Zn[II] *meso*-tetrakis(N-methylpyridyl)porphyrin (ZnTMPyP, see Figure 1). Owing to the nominal C_4 symmetry axis normal to the macrocycle, ZnTMPyP has a small net dipole moment; with a single methanol (CH$_3$OH) axially ligated to the Zn[II] ion; the calculated dipole moment is only 0.66 D (see Figure 1). ZnTMPyP is nevertheless soluble in a range of polar solvents because the peripheral N-methylpyridyl rings each carry a positive charge. Because the π-electron density in the ground state (see Figure 1a) is mostly confined to the region of the porphyrin, however, the resonance Raman active solvent molecules are effectively

held at some distance from the peripheral charges, so charge-dependent terms will make only a small contribution to the intermolecular potential. In short, the ground-state intermolecular mode frequency in ZnTMPyP solution should be smaller than detected in the same solvents in BChl solution because the only terms in the intermolecular potential that will make large contributions are those that depend on the polarizability of the porphyrin: the London-dispersion and solvent-dipole−induced-dipole terms.

The results show that the vibrational coherence from ZnTMPyP detected with Soret-band excitation contains dominant contributions from rapidly damped features arising from intermolecular modes with clustered solvent molecules. The components arising from intramolecular modes, from the porphyrin macrocycle proper or from the metal−axial-ligand interaction, can be distinguished from the intermolecular modes because they exhibit long damping times and narrow lineshapes. The intermolecular mode frequency follows the expected dependence on the solvent's dipole moment; the 70 cm^{-1} frequency in the nonpolar limit and the observation of a isotope shift in perdeuterated methanol are consistent with the hypothesis discussed above. In addition to supporting a structural assignment of the low-frequency modes that are coupled to the electron-transfer reactions in photosynthetic reaction centers, the results have additional significance because they suggest a role for intermolecular modes in the stabilization of charged intermediates in redox catalysis in proteins.

2. Experimental Section

Sample Preparation. ZnTMPyP (CAS 28850−44−4) was used as received from Sigma-Aldrich. CH$_3$OH (spectrophotometric grade) and CD$_3$OD (99.8 atom % D) were obtained from Sigma-Aldrich. CH$_3$OD (99 atom % D) was obtained from Cambridge Isotope Laboratories. Acetonitrile (CH$_3$CN, from Mallinckrodt, spectrophotometric grade), dimethylsulfoxide (DMSO, from EMD, ACS grade), and N,N-dimethylformamide (DMF, from Jade Scientific, reagent ACS grade) were used as received.

For use in the femtosecond pump−probe experiments, solutions of ZnTMPyP were prepared by dissolving the dry ZnTMPyP powder in the indicated solvent to obtain an

Vibrational Coherence in Polar Solutions

J. Phys. Chem. B, Vol. 113, No. 17, 2009 **6129**

absorbance of 0.4 for a path length of 1.0 mm at the center of the laser spectrum at 420 nm, as detailed below; with the methanols and DMSO, the solution was passed through a 0.22 μm microfilter prior to checking the absorbance. The samples were held in the femtosecond pump−probe spectrometer at room temperature (23 °C) in a fused-silica flow cuvette (0.5 mm path length). A peristaltic pump was used to circulate a 10 mL reservoir of sample solution through the cuvette at 2.75 mL/min. The sample's absorption spectrum was monitored during the experiment for changes arising from photochemistry or permanent photobleaching. The sample reservoir was exchanged with fresh solution several times during each run.

Continuous-Wave Absorption and Fluorescence Spectroscopy. Absorption spectra were obtained at 23 °C with a Hitachi U-2000 spectrophotometer (2 nm band pass). Fluorescence spectra were acquired at 23 °C with a Hitachi F-4500 spectrofluorimeter (5 nm band pass for the excitation and emission monochromators). As presented as a function of wavenumber, the fluorescence intensities are multiplied by the square of the wavelength in order to compensate for the fixed (in wavelength units) spectral bandpass of the emission spectrometer.[33]

Femtosecond Spectroscopy. Femtosecond pump−probe transients with impulsive excitation were recorded using the dynamic-absorption technique[29,31,34−36] with a pump−probe spectrometer consisting of a frequency doubled, self-mode-locked Ti:sapphire oscillator (Coherent Mira-F oscillator and Verdi V5 (5 W) Nd:YVO$_4$ pump laser, Coherent/Inrad 5-050 second-harmonic generator), a SF10 Brewster prism-pair pulse compressor, and a rapid-scanning, modified Mach−Zehnder interferometer with confocal sample and autocorrelation-crystal positions. The present experiments employ 50 fs pulses with intensity spectra centered at 420 nm (4 nm fwhm, as measured with an Ocean Optics USB-2000 spectrometer/CCD detector with a 0.5 nm bandpass), and a fairly narrow bandpass (0.5 nm) of the transmitted probe beam. This approach corresponds to that used by Champion and co-workers in their studies of low-frequency vibrational coherence in heme proteins.[37−39] In the present experiments, calcite polarizers in the pump and probe beams set the planes of polarization to be 45° apart; after passing through the sample, the probe beam was analyzed by another calcite polarizer at 90° relative to the pump-beam's plane of polarization, and then it passed through a monochromator (Acton Research SP-150) and was detected by an amplified photodiode (Thorlabs PDA55). The pump−probe signal was obtained from the photodiode signal using a lock-in amplifier (SRS SR-850); the pump beam was modulated at 100 kHz by a $\lambda/2$-retarding photoelastic modulator (Hinds Instrumentation) and a calcite polarizer. Aside from modifications to the pump−probe interferometer that allowed it to be operated in the 350−500 nm regime, the instrumentation and methodology is the same as that described in the previous work on BChl solutions and the B820 and B777 proteins.[21−23]

3. Results

Figure 2 shows continuous-wave absorption and fluorescence spectra from ZnTMPyP in methanol (CH$_3$OH) at 23 °C. The spectra are plotted as relative dipole strengths[33,40,41] as a function of wavenumber ν, $A(\nu)/\nu$ and $F(\nu)/\nu^3$, respectively. The absorption spectrum features two bands, the Soret (or B) band and the Q band, in the blue and red parts of the spectrum, respectively. The fluorescence spectrum extends to the red of the Q band. Figure 3 shows the solvent dependence of the Soret-band region from solutions of ZnTMPyP in CH$_3$OH, dimethylformamide (DMF), acetonitrile (CH$_3$CN), and dimethylsulfoxide (DMSO)
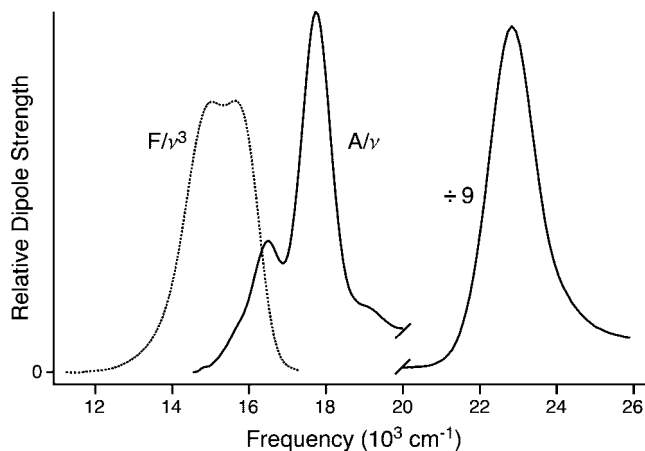

Figure 2. Soret ($\nu > 20000$ cm^{-1}) and Q-band region of the continuous-wave absorption (solid curve) and fluorescence (dotted curve) spectra from ZnTMPyP in CH$_3$OH at room temperature (23 °C), plotted as the dipole strength, A/ν and F/ν^3, respectively, and normalized to unit area with respect to the fluorescence spectrum and Q band.
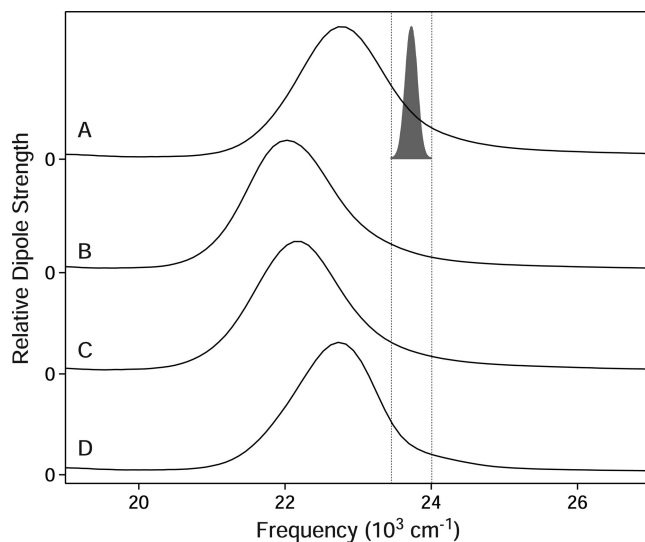

Figure 3. Soret-band absorption absorption dipole-strength (A/ν) spectra from ZnTMPyP in (a) CH$_3$OH, (b) DMF, (c) CH$_3$CN, and (d) DMSO. Superimposed with arbitrary scaling on (a) is the intensity spectrum of the 420 nm, 50 fs pulses used in all of the pump−probe experiments.

at 23 °C. Also shown in Figure 3 is the output spectrum from the frequency doubled Ti:sapphire oscillator as it was tuned for the dynamic-absorption experiments to 420 nm. The detected probe bandpass was obtained from the red side of the laser spectrum (422 nm).

The dynamic-absorption transients obtained from the ZnTMPyP solutions under these experimental conditions are shown in Figure 4. Following an intense coherence spike that goes off the plotted scale,[42−44] the transients exhibit a pattern of cosinusoidal modulations nearly all the way to the end of the 25 ps recording that is superimposed upon a single or double exponential decay function. The modulation pattern includes a strong very low-frequency component with positive-going recurrences at ~2 ps and ~18 ps; this oscillation carries a less intense set of higher frequency modulations that are even more slowly damped. Lastly, a very rapidly damped modulation contributes primarily to the 250−600 fs region of the transient. This portion of the signal is similar in character to the rapidly damped vibrational coherence observed in polar solutions of
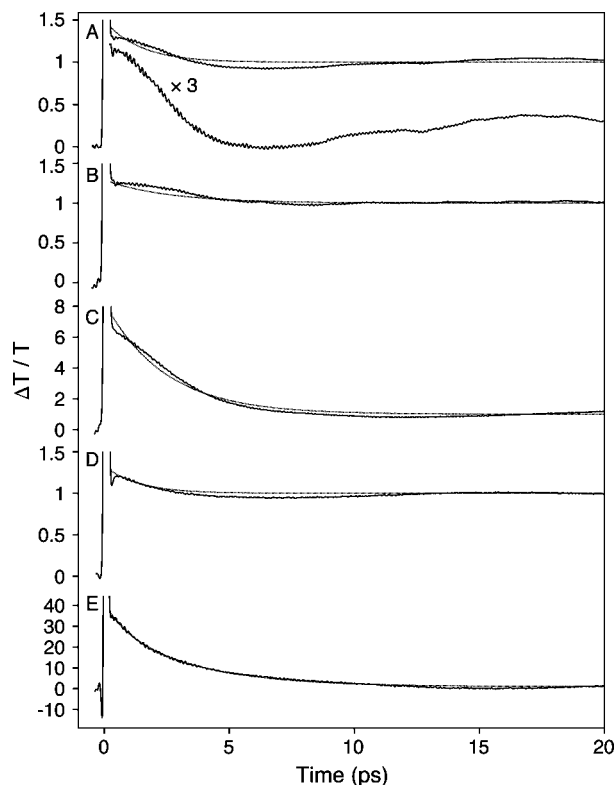
Figure 4. Femtosecond pump–probe dynamic-absorption transients detected at 422 nm (0.5 nm bandpass) with ZnTMPyP solutions in (a) CH$_3$OH, (b) CD$_3$OD, (c) DMF, (d) CH$_3$CN, and (e) DMSO. The >250 fs portion of the signal in CH$_3$OH is also shown in a ×3 expanded view. The signal traces are shown superimposed on single- or double-exponential fit functions of the form $A_0(1 + A_1e^{-t/\tau_1} + A_2e^{-t/\tau_2})$ for the 250 fs, 25 ps range. The fit parameters are provided in Table 1. As plotted, the signals are normalized by dividing by the nondecaying fraction, A_0.

TABLE 1: Model Parameters[a] for the Exponential Decays in the Pump–Probe Transients[b] in ZnTMPyP Solutions at 22 °C

solvent	A_1	τ_1 (ps)	A_2	τ_2 (ps)
CH$_3$OH	0.194	1.4		
CD$_3$OD	0.260	2.5		
DMF	2.32	2.4		
CH$_3$CN	0.160	1.2	0.293	1.4
DMSO	1.64	0.8	5.78	3.2

[a] See eq 1. [b] See Figure 4.

BChl, where the slowly damped portion of the signal is perhaps ten times weaker than observed in the ZnTMPyP transient.[22]

The dynamic-absorption signals from ZnTMPyP were fit in the time domain to a model consisting of a single- or double-exponential decay and an oscillatory portion containing slowly and rapidly damped parts. The models used previously with the signals observed in BChl solution and in the B820 or B777 systems were intended to handle only the rapidly damped components in the modulation pattern.[21−23] After truncation of the signal prior to the 250 fs delay point in order to avoid contributions from the tail of the coherence spike and from nonresonant background signals,[44] the oscillatory part was isolated by subtracting a fitted single- or double-exponential function:

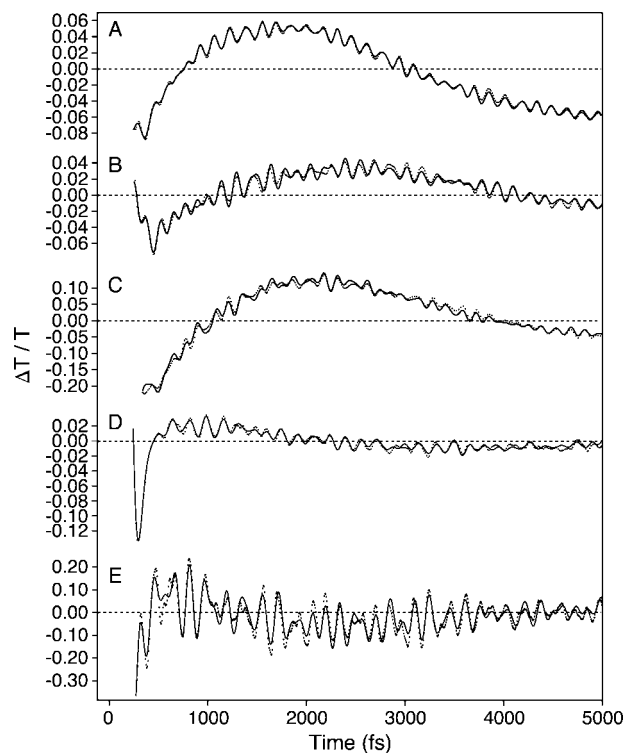$$I(t) = A_0\left(1 + A_1 e^{-t/\tau_1} + A_2 e^{-t/\tau_2}\right) \tag{1}$$

Figure 5. Oscillatory signals obtained from the pump–probe transients from ZnTMPyP solutions (see Figure 4) as the difference between the normalized signal and the fitted exponential decay functions in (a) CH$_3$OH, (b) CD$_3$OD, (c) DMF, (d) CH$_3$CN, and (e) DMSO. The data points are shown superimposed on a time-domain model composed of slowly damped and rapidly damped components (see eqs 2–6). The model parameters are listed in Tables 2 and 3.

The fit parameters are listed in Table 1. The transients and fits were normalized by dividing by A_0 in order to compare the amplitude of the modulation components to the intensity of the pump-induced ground-state depletion signal, which is effectively constant on the 0–25 ps time scale.

The oscillatory residuals, the difference between the normalized signal and the fitted decay function, were then fit by a multicomponent model that contains both slowly damped and rapidly damped oscillatory components (see Figure 5). The slowly damped part was modeled over the 250–7000 fs range as a sum of damped cosinusoids of the form

$$I_i(t) = A_i e^{-t^2\sigma_i^2/2}\cos(\omega_{0i}t - \phi_i)/\sqrt{2\pi} \tag{2}$$

with each modulation component i having a center frequency ω_{0i} and phase ϕ_i. These waveforms correspond to Gaussian lineshapes in the frequency domain,

$$I_i(\omega) = A_i e^{-(\omega - \omega_{0i})^2/(2\sigma_i^2)}/(\sigma_i\sqrt{2\pi}) \tag{3}$$

where the line width is controlled by the standard deviation, $\sigma_i = \Delta\omega_i/2\sqrt{(2\ln 2)}$, with $\Delta\omega_i$ representing the full width at half-maximum. eqs 2 and 3 are normalized so that the amplitude A_i corresponds to the area of the line shape in the frequency domain and to the intensity of the signal in the time domain; eq 2 corresponds to the Fourier transform of eq 3. As discussed below, an approximate description of the signal can be obtained with components described by exponentially damped cosinusoids,

Vibrational Coherence in Polar Solutions

J. Phys. Chem. B, Vol. 113, No. 17, 2009 **6131**

$$I_i(t) = A_i e^{-t/\gamma_i} \cos(\omega_{0i} t - \phi_i) \tag{4}$$

which correspond to Lorentzians in the frequency domain, but a poorer fit to the signal was obtained especially at long delays t; the model walks out-of-phase with respect to the experimental signal, and the time dependence of the amplitude is poorly described.

The rapidly damped part of the oscillatory residuals (Figure 5) was modeled in the time domain as the sum of two inhomogeneously broadened components with asymmetric Gaussian lineshapes. We showed previously that such a model provides a good description of the rapidly damped vibrational coherence from BChl in polar solution;[21,22] the reader is directed to that work for a detailed discussion and for tests of the model. The two rapidly damped components are assigned, in order of frequency, to the hindered translational and librational (hindered rotational) intermolecular modes between the porphyrin or chlorophyll macrocycle and its clustered, first-solvation-shell solvent molecules.[22,45,46]

In the work on BChl solutions, each rapidly damped component was described in the time domain by an integral over a distribution of exponentially damped cosinusoids with an intrinsic (or homogeneous) damping time γ; the intensities of the cosinusoids are scaled by a log-normal line shape,[47] $\mathscr{L}(\omega)$:

$$I_i(t) = \int_0^\infty d\omega \, \mathscr{L}(\omega) \cos(\omega t - \phi_i) \, e^{-t/\gamma} \tag{5}$$

$\mathscr{L}(\omega)$ is parametrized by its area, A_i, its center frequency, ω_{0i}, its width, $\Delta\omega_i$, and an asymmetry (or skew) parameter, ρ_i.

In the present work, the $\mathscr{L}(\omega)$ distribution function was approximated with the piecewise sum of two half-Gaussian lineshapes, $\mathscr{G}(\omega, A_i, \omega_{0i}, \sigma_i, \rho_i)$, and the integral is replaced by a sum over an evenly spaced set of sub-Gaussian components $I_j(t)$ of width $\sigma_i/4$ spaced by $\sigma_i/2$:

$$I_i(t) = \sum_{j=0}^{22} \mathscr{G}(\omega_{0j} = \omega_{0i} + (j - 8)\sigma_j, A_i, \omega_{0i}, \sigma_i, \rho_i) \times$$
$$I_j(t, \omega_{0j}, \sigma_j = \sigma_i/4) \tag{6}$$

The j sub-Gaussians are expressed in the time and frequency domain by expressions analogous to eqs 2 and 3; in the sum, they are scaled by the intensity of $\mathscr{G}(\omega)$ sampled at their center frequencies, ω_{0j}. The right- and left-side widths $\sigma_{r,l}$ of $\mathscr{G}(\omega)$ are determined by the overall width of the distribution σ_i and its asymmetry ρ_i as

$$\sigma_i = (\sigma_l + \sigma_r)/2 = \sigma_l(1 + \rho_i)/2 \tag{7}$$

The widths σ_r and σ_l are related by $\rho_i = \sigma_r/\sigma_l$; the left- ($l$) and right-hand ($r$) half-Gaussians are defined by eq 3 over $\omega < \omega_{0i}$ and $\omega \geq \omega_{0i}$, respectively. Note that the choice of the width and spacing of the sub-Gaussians determines the number required (here, 23) to obtain a smooth approximation of a log-normal distribution. The sum in eq 6 was truncated at 0 cm^{-1}, if necessary, in order to avoid the addition of negative frequencies to the waveform, and it was normalized so that the area of the line shape in the frequency domain was set to the amplitude parameter A_i. The resulting rapidly damped waveform and line shape are indistinguishable from those obtained in previous work for a given set of parameters, but the nonlinear

TABLE 2: Solvent Dependence of the Asymmetric Gaussian Lineshape Parameters for the Rapidly Damped Components Observed in the Vibrational Coherence from ZnTMPyP

		Solvent				
component	parameter[a]	CH$_3$OH	CD$_3$OD	DMF	CH$_3$CN	DMSO
1	ω_0, cm^{-1}	68	63	82	80	100
	$\Delta\omega$, cm^{-1}	49	55	59	50	48
	A^b	9.81	10.1	7.67	69.8	62.2
	ρ	1.18	1.17	1.45	1.21	1.17
2	ω_0, cm^{-1}	81	73	94	119	124
	$\Delta\omega$, cm^{-1}	59	45	50	59	56
	A^b	15.1	17.2	8.10	82.3	125
	ρ	1.18	1.18	1.29	1.15	1.55
Sum	$\langle\omega\rangle$, cm^{-1}	79	74	95	106	125
	$\Sigma_i A_i$	24.9	27.3	15.8	152	187

[a] See eqs 2–6 and the text. [b] Normalized to the intensity of the $\sim$215 cm^{-1} slowly damped component in each solvent.

optimization program runs perhaps 2 orders of magnitude faster than before because the log-normal line shape function itself[47] is avoided and the number of sub-Gaussians in the sum is small. A further benefit is that no assumption of the intrinsic damping time γ is required; a Raman echo experiment would be required to obtain a discrete measurement of the homogeneous linebroadening.[48,49]

The slowly and rapidly damped portions of the signal were modeled separately in order to simplify the optimization procedure. The slowly damped part of the residual oscillatory signal was modeled first using a set of components constrained to have narrow lineshapes ($\Delta\omega_i < 10$ cm^{-1}). Starting frequencies and widths for these components were obtained from a Hanning-windowed Fourier-transform spectrum (see Figure 6); the window function attenuates the rapidly damped portion of the signal.[50] The 12 most intense components in the Fourier-transform spectrum were included in the slowly damped part of the model. The converged model produced a Hanning-windowed Fourier transform spectrum that matched the experimental spectrum; the frequencies, widths, and relative amplitudes are particularly well-defined because the linewidths are narrow. The rapidly damped model discussed above was then constrained during the second phase of the optimization process to return only broad lineshapes ($\Delta\omega_i > 10$ cm^{-1}). In all the solvents studied, the sum of two rapidly damped asymmetric Gaussian components provided a good description of the rapidly damped residual function.

The sum of the rapidly damped and slowly damped models is superimposed on the data points in Figure 5. Both the slowly damped and rapidly damped portions of the model were found to be robust with respect to the starting parameters used in both parts of the nonlinear optimization procedure. The final fitted amplitudes A_i have estimated confidence intervals that are no worse than $\pm 5\%$, and the center frequencies ω_{0i} are known with confidence intervals of ± 2 cm^{-1}. The parameters for the optimized time-domain models shown in Figure 5 are tabulated in Table 2 and Table 3. The tabulated amplitudes A_i are normalized with respect to the intensity of the ground-state depletion part of the signal (see the ordinate scaling for Figure 4) and to the amplitude for the $\sim$215 cm^{-1} component, the strongest slowly damped, high-frequency ($\omega_{0i} > 100$ cm^{-1}) component in all of the solvents but DMSO, where the 195 cm^{-1} component is the strongest.

Effective exponential damping times for the Gaussian or asymmetric Gaussian modulation components were estimated by fitting an exponentially damped cosinusoid (see eq 4) to the

TABLE 3: Gaussian Lineshape Parameters[a] for the Slowly Damped Modulation Components Observed in ZnTMPyP Pump−Probe Transients

	solvent				
component	CH_3OH	CD_3OD	DMF	CH_3CN	DMSO
1	3, 3.47, 25	3, 1.74, 12	2, 10.6, 77	3, 3.66, 3.2	4, 3.14, 2.9
2	21, 8.88. 1.5	23, 16.8, 1.2	19, 6.87, 2.4	19, 11.8, 1.5	13, 2.37, 0.41
3	38, 2.03, 0.16	29, 2.35, 0.32	43, 3.13, 0.22	47, 0.697, 0.15	46, 2.40, 0.19
4	89, 2.39, 0.096	85, 2.35, 0.13	76, 417, 0.39	79, 1.00, 0.27	93, 4.18, 0.28
5	138, 2.78, 0.071	131, 2.35, 0.064	134, 8.24, 2.0	131, 2.01, 0.23	148, 2.86, 0.21
6	177, 2.96, 0.21	177, 4.05, 0.75	174, 2.01, 0.090	172, 2.42, 0.41	177, 3.19, 1.4
7	191, 2.78, 0.31	190, 4.23, 0.53	188, 2.52, 0.091	186, 4.45, 0.81	195, 5.88, 1.7
8	215, 1.67, 1.0	214, 1.77, 1.0	212, 3.35, 1.0	213, 3.53, 1.0	214, 2.56, 1.0
9	244, 1.90, 0.13	244, 2.35, 0.15	240, 2.25, 0.81	241, 2.34, 0.18	249, 2.36, 0.52
10	264, 3.62, 0.43	263, 7.06, 1.5	259, 3.16, 0.13	263, 3.02, 0.14	262, 4.24, 1.5
11	284, 3.16, 0.42	279, 6.04, 0.12	278, 3.28, 0.17	277, 4.17, 0.020	290, 4.48, 0.13
12	312, 3.24, 0.19	311, 2.06, 0.20	306, 4.91, 0.89	312, 3.93, 0.17	314, 1.61, 0.20
A_8[b]	0.016	0.016	0.025	0.015	0.089

[a] (ω_0, cm^{-1}; $\Delta\omega_0$, cm^{-1}; A_i); see eqs 2−6 and the text. The amplitudes A_i are normalized by that of component 8. [b] Raw amplitude for component 8 relative to normalized pump−probe transient (see Figure 4).
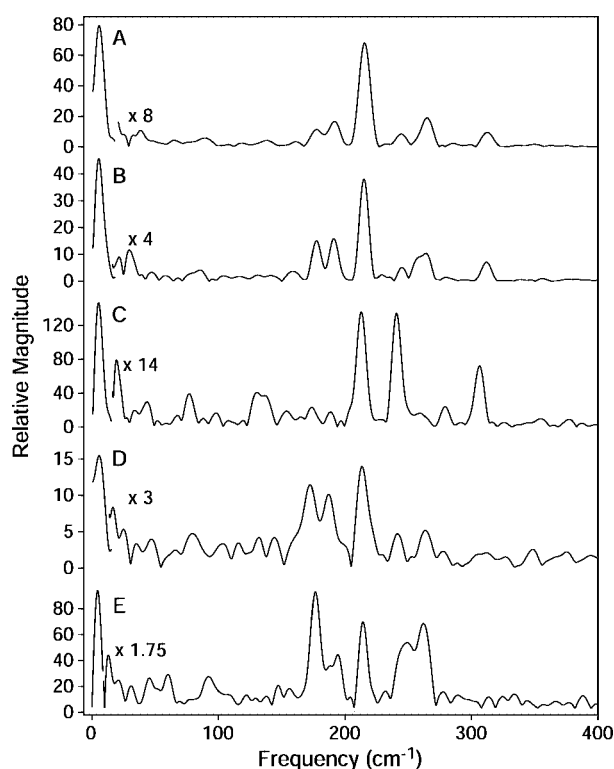

Figure 6. Fourier transform magnitude spectra from the oscillatory residuals (see Figure 5) of the pump−probe signals from ZnTMPyP solutions in (a) CH_3OH, (b) CD_3OD, (c) DMF, (d) CH_3CN, and (e) DMSO. The Fourier transform was applied to the oscillatory input signals after a Hanning window was applied over the 250−7000 fs range.

TABLE 4: Comparison of Gaussian Linewidths and Effective Exponential Damping Times[a] for the Modulation Components Observed in the Vibrational Coherence from ZnTMPyP in CH_3OH

ω_0, cm^{-1}	$\Delta\omega$, cm^{-1}	γ, ps
3	3.47	2.94[b,c]
21	8.88	1.36
38	2.03	6.71[c]
68[d]	49	0.223
81[d]	59	0.182
89	2.39	5.64
138	2.78	4.85
177	2.96	4.57
191	2.78	4.87
215	1.67	8.14[c]
244	1.90	7.16
264	3.62	3.58
284	3.16	4.11
312	3.24	4.16

[a] See eq 4 and Figure 7. [b] Lower limit; an upper limit of $\gamma = 21.6$ ps is obtained by fitting to the $t > 15$ ps portion of the signal. [c] See Figure 7. [d] Rapidly damped component, see eq 6 and the text.

if the Lorentzian waveform is constrained to fit the Gaussian waveform at the end of the modulation pattern, the resulting damping time is longer. This issue is especially important for the slowly damped 3 cm^{-1} asymmetric Gaussian component, which exhibits a 2.94 ps damping time if the overall waveform is fitted, but if the fit is constrained to the >10 ps region, a 21.6 ps damping time is obtained. As mentioned above, we find that Lorentzian waveforms result in a poor overall model for the oscillatory residuals even if constrained over the 250−7000 fs region, so the damping times in Table 4 have to be regarded as crude lower-limit estimates of the damping time. Given that Gaussian lineshapes are observed, and that these lineshapes inherently report inhomogeneous broadening, the true homogeneous damping times may be significantly longer.

Figure 8 shows the frequency domain representation of the overall time-domain model for the oscillatory residuals shown in Figure 5. The spectra are dominated by the broad lineshapes from the rapidly damped components over the 50−200 cm^{-1} region. The slowly damped component whose line shape is centered at 2−4 cm^{-1} is, however, comparable in intensity to the sum of the two rapidly damped components (see Table 2 and Table 3). The other slowly damped components are an order of magnitude less intense.
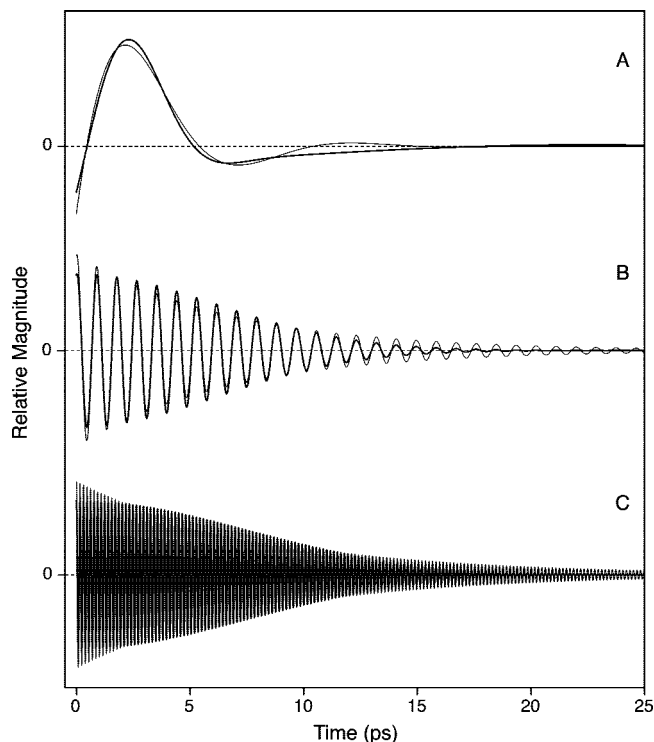
Gaussian waveform for each component in the model. This exercise corresponds in the frequency domain to optimizing a Lorentzian line shape to the corresponding Gaussian line shape. As an example, the Gaussian linewidths, $\Delta\omega_0$, and the exponential damping times, γ, are compared for ZnTMPyP in CH_3OH in Table 4; similar results (not shown) are obtained in the other solvents. Figure 7 compares the Gaussian and fitted Lorentzian waveforms for the 3, 38, and 215 cm^{-1} components. The Lorentzian waveforms were optimized over the 250−7000 fs range, as in Figure 5, but the results are comparable when the entire 250−25000 fs range shown in Figure 7 is fit. In general, the fitted Lorentzian waveform is more intense than Gaussian waveform at the beginning and end of the waveform;

Figure 7. Comparison of the Gaussian waveforms (thick curves) obtained for the 3, 38, and 215 cm^{-1} components in the oscillatory signals observed from ZnTMPyP in CH$_3$OH solution with fitted exponentially damped waveforms (thin curves, see eq 4). The Gaussian linewidths and damping times are listed in Table 4.

Figure 9. Time-domain representation of the rapidly damped oscillatory components (see Figures 5 and 8) in the pump−probe signals from ZnTMPyP solutions in (a) CH$_3$OH, (b) CD$_3$OD, (c) DMF, (d) CH$_3$CN, and (e) DMSO. The dotted portion of the signal is extrapolated from the fitted region of time (see Figure 5).

Figure 9 shows a time-domain representation of the summed rapidly damped components from the models shown in Figure 5. Because the effective damping time for both of the rapidly damped components is <250 fs in all of the solvents, a great deal of the amplitude of this component lies in the early time truncated portion of the pump−probe transient (see Figure 4 and Figure 5). As extrapolated in Figure 9, the waveforms in CH$_3$OH and CD$_3$OD are very similar to the rapidly damped vibrational coherence observed previously in polar solutions of BChl, where the intramolecular, slowly damped vibrational coherence is comparatively weak.[21,22] The strong positive-going recurrence at ∼200 fs for the waveform in CH$_3$OH is only partially observed in the analyzed time region of the residual; a weaker second recurrence at ∼600 fs is followed by a broad negative-going trough at ∼900 fs that recovers to the baseline over the 1000−1500 fs range. As the solvent is varied, the extent in time of the rapidly damped waveform contracts as the mean frequency, $\langle\omega\rangle$, increases (see Figure 9). From the sum of the two underlining component lineshapes (see Figure 8), $\mathscr{M}(\omega) = I_1(\omega) + I_2(\omega)$, the mean frequency obtained using a normalized mean-value relation,

$$\langle\omega\rangle = \frac{\int_0^\infty d\omega\,\mathscr{M}(\omega)\omega}{\int_0^\infty d\omega\,\mathscr{M}(\omega)} \tag{8}$$
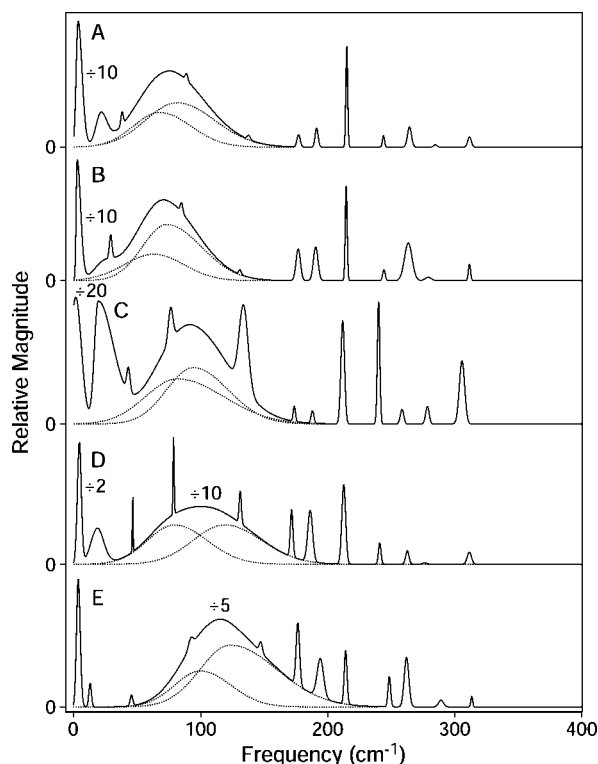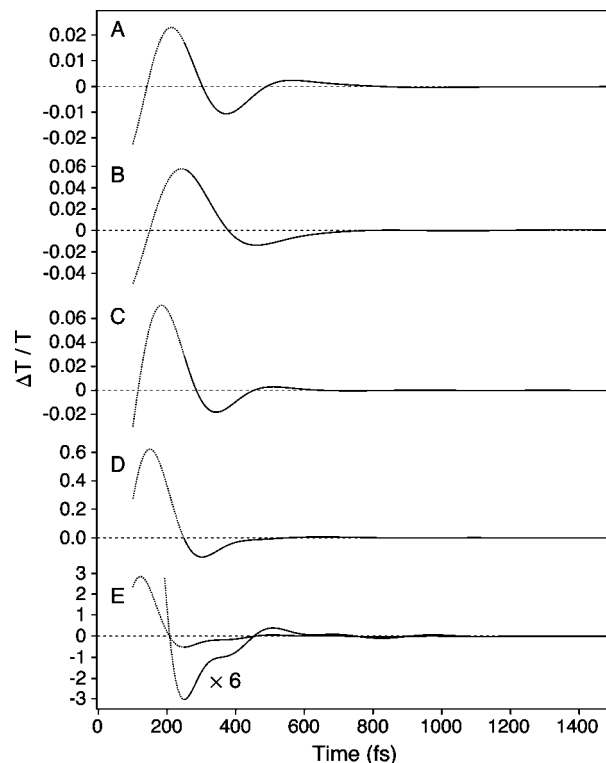

Figure 8. Frequency domain representation of the time-domain models of the oscillatory signals (see Figure 5) observed in ZnTMPyP solution in (a) CH$_3$OH, (b) CD$_3$OD, (c) DMF, (d) CH$_3$CN, and (e) DMSO. The broad features in the 50−200 cm^{-1} regime are shown superimposed with the spectra (dotted lines) of their underlying components; in (d) and (e) these features are attenuated in order to keep them on scale. The spectrum from the 2−4 cm^{-1} slowly damped component in (a−d) is also attenuated.

shifts over the 79−125 cm^{-1} range as the solvent is varied (see Table 2 and Figure 10). As compared with those observed in CH$_3$OH, the spectra of the two rapidly damped components in CD$_3$OD (see Figure 8) are downshifted by 5 and 8 cm^{-1} and the mean frequency is downshifted by 5 cm^{-1} (see Table 2).
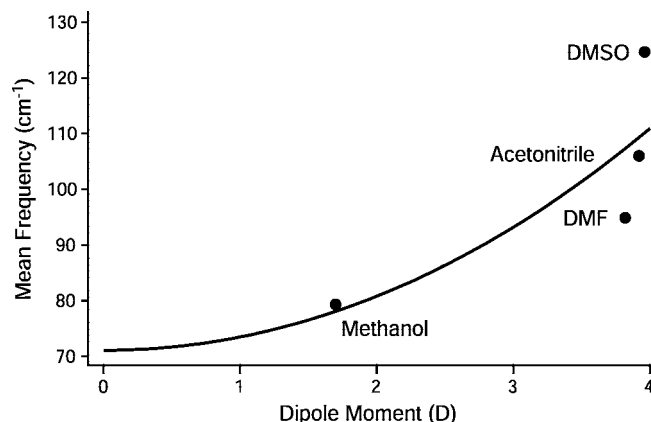
Figure 10. Dependence of the mean frequency of the rapidly damped oscillatory components (see Figures 5 and 8) observed in the pump—probe signals from ZnTMPyP solutions in CH_3OH, DMF, CH_3CN, and DMSO. The data points are shown superimposed with a trend fitted to eq 12.

4. Discussion

The femtosecond pump—probe, dynamic-absorption transients obtained with Soret-band excitation of polar solutions of ZnTMPyP (see Figure 4) exhibit a complex modulated signal superimposed on an exponential or double-exponential decay function with a ~2 ps time constant leading to a nondecaying offset over the 0—25 ps time range. Similar decay components and time constants are attributed to the $S_2 \rightarrow S_1$ internal-conversion process in pump—probe or fluorescence-upconversion experiments with Zn^{II} tetraphenylporphyrin (ZnTPP) in nonpolar solvents,[51,52] but for ZnTMPyP in polar solvents, the decays arise from vibrational relaxation and vibrational energy transfer to the solvent in the S_1 state following an ultrafast ($\tau \leq 100$ fs) internal-conversion process. In femtosecond transient-absorption experiments employing continuum probe pulses and 150 fs pump pulses in the Soret band at 404 nm, Fontaine-Aupart and co-workers[53] failed to detect an S_2-state stimulated-emission band from ZnTMPyP in aqueous solution, so the S_2-state population relaxes to the S_1-state vibronic manifold almost as rapidly as it is prepared by the pump pulse. In contrast, a distinct stimulated-emission band was observed for ZnTPP under the same optical conditions; the intensity of the stimulated emission decays with a 2 ps time constant as the S_2-state population relaxes to the S_1-state. In ZnTMPyP, population deposited in excited vibronic levels of the S_1-state manifold by the $S_2 \rightarrow S_1$ internal-conversion process is detected in terms of excited-state absorption (ESA) transitions to vibronic levels in the Soret band (states S_n). The time-resolved pump—probe spectra observed by Fontaine-Aupart and co-workers exhibit a broad-region of long-lived (>5 ps) excited-state absorption at wavelengths above 450 nm; the relatively sharp, ground-state depletion band that lies to the blue has a maximum at 435 nm and extends to ~405 nm.[53] At wavelengths below 435 nm, however, it is likely that the ground-state depletion and ESA bands overlap extensively. Thus, in our experiments, the net ground-state depletion signal decreases in intensity as the S_1-state population cools on the picosecond time scale because the ESA band shifts to the blue and overlaps more strongly with the static ground-state depletion band at the 422 nm probe bandpass.

The intensity of the decays we observe in the ZnTMPyP pump—probe signals are solvent dependent, and the decay in two of the solvents (CH_3CN and DMSO) is biexponential. The decays observed for ZnTMPyP in DMSO and CH_3OH are not

significantly altered (not shown) when the laser is tuned to 425 nm, closer to the Soret band's maximum but still on the blue side. These observations show that the observed dynamics are less dependent on the initial vibronic state prepared in the S_2-state manifold than they are on the nature of the solvent. Given that dynamic solvation does not contribute to the signal because the S_2 state persists for such a short period following absorption of the pump pulse, the rate at which the excess vibrational energy of the S_1 state is dissipated is solvent dependent. Biexponentiality would arise in this case from the presence of two ensembles of ZnTMPyP with different first-solvation shell structures. A similar explanation was invoked by Zewail and co-workers to account for the biexponential internal conversion for ZnTPP in methylene chloride.[51]

The conclusion that the S_2 state of ZnTMPyP decays to the S_1 state via an internal-conversion process on the ≤ 100 fs time scale is especially significant with respect to the present work because it restricts assignment of the modulation components observed in the pump—probe signals to coherent wavepacket motions on the ground-state potential-energy surface. Table 4 shows that all of the slowly damped modulation components have effective damping times that are >1 ps; even the two rapidly damped components have effective damping times that are >150 fs. It is unlikely that the ESA transitions that overlap with the probed region of the spectrum contribute to the modulated signal; the $S_2 \rightarrow S_1$ internal-conversion process would be expected to be incoherent with respect to the initial vibrational phase prepared by the pump pulses.[54]

Except for the 2—4 cm^{-1} component, the modulation components with the largest amplitudes A_i are observed in the 200 cm^{-1} region of the spectrum. This pattern of amplitudes is consistent with an assignment to coherent wavepacket motions on the ground-state potential energy surface because these experiments employed 50 fs pump pulses. If the ground- and excited-state potential-energy surfaces of the system are displaced with respect to the coordinate of a normal mode of vibration, moving wavepackets on the ground- and excited-state potential surfaces are generated by two successive actions of the pump field.[27,28,30,31] The ground-state wavepacket is created by a process that directly corresponds to resonance Raman scattering. The duration of the pump pulse controls the displacement and momentum of the ground-state wavepacket because it places a limit on the time interval between the first action of the pump field that prepares the ground—excited-state polarization and the second action that materializes the wavepacket on the ground-state surface. The pump—probe signal is modulated optimally by ground-state wavepacket motion when the pump—pulse duration is about one-third of the mode's period; with pulses that are shorter than the optimum, the wavepacket is not displaced very far away from the Franck—Condon geometry, so only a small modulation of the transmitted probe signal results. Of course, the depth of modulation of the pump—probe signal decreases as the pump—pulse duration increases beyond the optimum duration toward the mode's period.[30] With the 50 fs pulses used in the present experiments, the optimum mode frequency is 222 cm^{-1}; the relative strength of the ~215 cm^{-1} component observed in each solvent is probably due to the close matching of the pump—pulse duration with the mode frequency. Even though the measured amplitude of the 312 cm^{-1} mode is only about one-fifth that of the 215 cm^{-1} mode (see Table 3), the relative resonance Raman activities of the two modes are comparable if one considers that the optimum pulse duration that would drive a 312 cm^{-1} wavepacket is ~32 fs.

Vibrational Coherence in Polar Solutions

J. Phys. Chem. B, Vol. 113, No. 17, 2009 **6135**

The unusually large amplitude of the very low frequency, $2-4$ cm^{-1} modulation component would seem to be in conflict with an assignment to a ground-state wavepacket motion. The modulation depth that would be expected with 50 fs pump pulses would be close to zero for such a low frequency mode unless it is characterized by an unusually large excited-state displacement. Most of the intramolecular vibrational modes of ZnTMPyP would be expected to exhibit comparable displacements, with the strongest modes associated with the π-electron density in the porphyrin macrocycle, so the rule-of-thumb about the optimum pulse duration discussed above would reasonably apply.[30] An exception might be anticipated for the internal rotation of the peripheral N-methylpyridyl rings (see Figure 1). In the ground state, the rings are rotated well away from the plane of the porphyrin; in the excited state, owing to the flow of the π-electron density from the porphyrin region, the minimum-energy geometry would extend the conjugated region by making the rings and porphyrin coplanar. Thus, an internal rotation of the rings is launched in the excited-state by resonant excitation of the Soret band because the S_2-state potential-energy surface is sloped in the Franck–Condon region along that coordinate; the internal rotation would obtain significant momentum prior to preparation of the ground-state wavepacket on the ground-state surface, where the rotation is bound only owing to the poor delocalization of the π-electron density and owing to steric hindrance. This assignment of the $2-4$ cm^{-1} mode is also prompted by its significant solvent dependence (see Table 3); the highest frequency (4 cm^{-1}) is observed in the most viscous solvent (DMSO), and perhaps the large amplitude in DMF relates to a specific clustering around the rings.

The frequencies, linewidths, and relative intensities of the other slowly damped modulation components are relatively insensitive to the choice of solvent (see Table 3). These components are well-modeled (see Figure 5) by relatively narrow Gaussian components (eq 2). The solvent independence of the modulation frequencies supports a structural assignment of all of these features to the intramolecular, skeletal modes of the Zn^{II}-porphyrin macrocycle. Normal-mode calculations using the B3LYP hybrid density functional for the ZnTMPyP–methanol complex (see Figure 1) are consistent with an assignment of the ~40 cm^{-1} and ~215 cm^{-1} components to the metal-doming and Zn^{II}–axial-ligand stretching modes, respectively; somewhat higher frequencies are assigned to these modes in Fe^{II}-porphyrins.[55] Of these, the former is evidently more solvent sensitive, but it should be kept in mind that the frequencies and intensities of the very lowest frequency components in the slowly damped set of features are known with less confidence than for the higher-frequency or more rapidly damped features. As compared with the amplitude of the rapidly damped components, the slowly damped components are much stronger in ZnTMPyP with Soret-band excitation than observed with Q-band excitation of BChl solution; the resonance Raman intensities of the intramolecular modes of porphyrins are strongly enhanced by excitation in the Soret band.[56]

The rapidly damped ($\gamma < 1$ ps) part of the vibrational coherence observed in ZnTMPyP solution exhibits solvent-dependent time-domain waveforms that are very similar to those observed in BChl solution. In the frequency domain, the two rapidly damped components present inhomogeneously broadened lineshapes that are analogous to the ones assigned to the hindered translational and librational modes in instantaneous normal-mode analyses of molecular dynamics simulations of polar liquids.[45,46,57] A structural assignment of these components to intermolecular modes between the Zn^{II}-porphyrin and the clustered solvent molecules in the first

solvation shell is directly supported by the observation of an isotope-dependent shift of frequencies in methanol and perdeuterated methanol solution (see Table 2 and Figure 8) of approximately the right magnitude. The mean frequency observed in CH_3OH is 79 cm^{-1}; in the harmonic-oscillator limit, if the mode involves an intermolecular mode between a single CH_3OH molecule and the ZnTMPyP molecule, the mode should exhibit a downshift to 74.7 cm^{-1} using the $\omega_D = \omega_H(\mu_H/\mu_D)^{0.5}$ relationship[58] between the frequency ω_D of the deuterated species and the frequency ω_H of the protonated species and their reduced masses μ_D and μ_H, respectively. The observation of a slightly lower mean frequency, 74 cm^{-1}, might indicate the presence of some higher molecular weight species, perhaps from hydrogen-bonded chains,[59–62] but the confidence interval (± 2 cm^{-1}) is larger than this discrepancy. Consistent with the intermolecular mode assignment, a smaller shift of frequencies occurs upon changing CH_3OH to CH_3OD (results not shown); the observed mean frequency of 76 cm^{-1} in CH_3OD is within the confidence interval of the expected value of 77.9 cm^{-1}.

As noted in the Introduction, the solvent dependence of the rapidly damped components (see Table 2 and Figure 8) provides a test of the form of the van der Waals potential introduced in the previous work on BChl solutions,[22]

$$V_0(r) = a/r^{12} - \left(b\alpha_1\alpha_2 + \frac{c|\pmb{\mu}_1|^2|\pmb{\mu}_2|^2}{(4\pi\varepsilon_0)^2} + \frac{\alpha_2|\pmb{\mu}_1|^2 + \alpha_1|\pmb{\mu}_2|^2}{4\pi\varepsilon_0} \right)/D^2 r^6 \quad (9)$$

A relation for the natural frequency of the intermolecular mode in the limit of small displacements from the equilibrium structure,

$$\nu = \frac{3}{(2a)^{2/3}} \left(b\alpha_1\alpha_2 + \frac{c|\pmb{\mu}_1|^2|\pmb{\mu}_2|^2}{(4\pi\varepsilon_0)^2} + \frac{\alpha_2|\pmb{\mu}_1|^2 + \alpha_1|\pmb{\mu}_2|^2}{4\pi\varepsilon_0} \right)^{7/6}/2\pi D^{7/3} \mu^{1/2} \quad (10)$$

is obtained from a Taylor series expansion of eq 9. Both expressions contain a series of terms arising from the physical components of the interaction: the constant a scales the Pauli exchange interaction, the London-dispersion interaction is scaled by the constant $b = 3I_1I_2/2(I_1 + I_2)$, with $I_{1,2}$ representing the ionization potentials for the two molecules, $c = 2/3k_BT$ scales the dipole–dipole interaction, and the $\alpha_2|\pmb{\mu}_1|^2$ and $\alpha_1|\pmb{\mu}_2|^2$ terms arise from the solute–dipole and solvent–dipole induced-dipole interactions, respectively.[63–66] In these equations, $\pmb{\mu}_i$ and α_i correspond to the dipole moment and polarizability for the solute (subscript 1) and solvent (subscript 2); r is the distance between the two molecules, μ is the reduced mass for the intermolecular oscillator, D represents the dielectric constant for the solvent, and ε_0 relates the permittivity of free space.

If the solute chromophore is charged, the intermolecular potential gains two additional terms, for the ion–dipole and ion–induced dipole interactions:

$$V_Q(r) = V_0 - \left(\frac{cQ|\pmb{\mu}_2|^2}{(4\pi\varepsilon_0)^2} + \frac{\alpha_2 Q^2}{4\pi\varepsilon_0} \right)/2D^2 r^4 \quad (11)$$
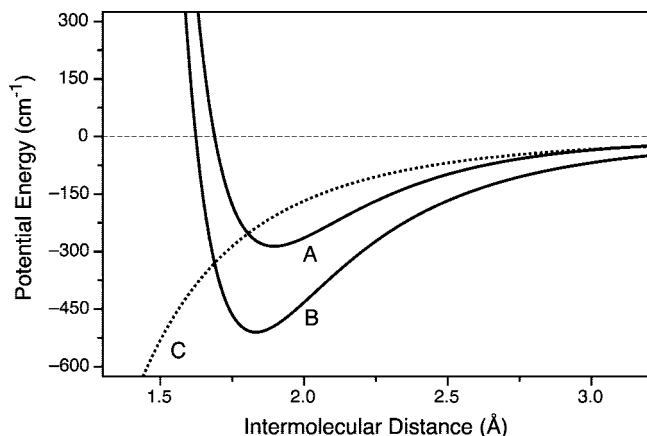
Figure 11. Model potential-energy curves for the ZnTMPyP–CH$_3$OH complex calculated using eq 11 and the experimentally observed mean intermolecular mode frequency, 79 cm^{-1} (see Table 2): (a) $Q = 0$; (b) $Q = 1$; and (c) the attractive, charge-dependent terms for $Q = 1$. Table 5 lists the other parameters for the potential curves and compares r_{eq} and V_{min} for curves (a) and (b).

TABLE 5: Parameters for the Model ZnTMPyP-CH$_3$OH Intermolecular Potentials Shown in Figure 11

parameter[a]	value
exchange (Pauli) interaction coefficient, a	76.2 eV Å^{12}
London-dispersion interaction coefficient, $b = 3I_1I_2/2(I_1 + I_2)$	9.35 eV[b,c]
ZnTMPyP dipole moment, $|\boldsymbol{\mu}_1|$	0.663 D[b]
CH$_3$OH dipole moment, $|\boldsymbol{\mu}_2|$	1.70 D[c]
ZnTMPyP polarizability, α_1	109.8 Å$^{3 \, b}$
CH$_3$OH polarizability, α_2	3.29 Å$^{3 \, c}$
ZnTMPyP-CH$_3$OH reduced mass, μ	30.7 Da
CH$_3$OH dielectric constant, D	33[c]
r_{eq} ($Q = 0$)	1.90 Å
V_{min} ($Q = 0$)	286 cm^{-1}
r_{eq} ($Q = 1$)	1.83 Å
V_{min} ($Q = 1$)	510 cm^{-1}

[a] See eqs 9 and 11 and the text. [b] From B3LYP 6−31G electronic structure calculation. [c] From ref 67.

The ion-dipole term depends linearly on the charge Q of the solute and on the square of the solvent's dipole moment, $\boldsymbol{\mu}_2$; the ion−induced-dipole term contains the polarizability α_2 of the solvent and the square of the charge, Q^2. Both terms depend on r^{-4}, so they decay much less rapidly with increasing distance than the rest of the terms in the intermolecular potential. The mode frequency expression that follows from eq 11 is too lengthy to be included here, but it predicts that the charge-dependent terms significantly increase the mode frequency over that predicted by eq 10.

Figure 11 shows a pair of model potentials for the ZnTMPyP−CH$_3$OH intermolecular mode that illustrates the effect of turning on the charge-dependent terms in eq 11 and of changing the intermolecular distance. The only parameter in the intermolecular potential that is not known from the literature, from a calculation, or from experiment is that for the exchange interaction, a, but it can be estimated given an experimental measurement of the mode frequency and an initial assumption of $Q = 0$ so that the charge-dependent terms are inactive. Combination of eqs 9 and 10 and the observed mean frequency of 79 cm^{-1} (see Table 2) returns a value for a of 76.2 eV Å^{12}; the rest of the parameters used in Figure 11 are listed in Table 5 along with estimates for the equilibrium bond distance, r_{eq}, and the bond-dissociation energy, V_{min}, with $Q = 0$ and $Q = 1$. If a is held constant, the effect of changing Q from 0 to 1 is a

sharpening of the potential near the minimum, which indicates an increased mode frequency, almost a doubling of V_{min}, and a modest 0.07 Å reduction in r_{eq} (compare curves (a) and (b) in Figure 11). Curve (c) in Figure 11 shows the magnitude of the charge-dependent terms in eq 11, as calculated for the $Q = 1$ potential. This curve can be used to gauge the contribution of the charged terms to the stabilization and mode frequency when the charges are located at some distance from the clustered solvent molecules. The ones that interact with the π-electron density in the ground state are those that contribute to the ground-state vibrational coherence, and on average, these solvent molecules are constrained to be more than 2.5 Å from the charges on the N-methylpyridyl rings. This distance estimate is based on the assumption that the charge is localized on the nearest carbon atom of the N-methylpyridyl ring and that the solvent molecule is fixed at r_{eq} for the $Q = 0$ case normal to the porphyrin ring above the adjacent *meso* carbon atom, to which the N-methylpyridyl rings are attached. At this distance, the charge-dependent terms account for a 70 cm^{-1} stabilization, about 25% of V_{min} for $Q = 0$. Given that the charge is actually delocalized over the N-methylpyridyl ring in the ground state, the integrated interaction energy will be considerably smaller than this worst-case estimate. We conclude that it is a good approximation to neglect the charge-dependent terms in the ground-state intermolecular potential. In the excited state, because the π-electron density is extensively delocalized from the porphyrin region onto the N-methylpyridyl rings, the intermolecular mode frequency should be significantly increased from that in the ground state owing to a larger contribution of the charge-dependent terms in eq 11.

The expression for the intermolecular mode frequency in the absence of charge-dependent terms, eq 10, can be simplified to give a relation for the dependence on the dipole moment of the solvent as

$$\nu = (C_1 + C_2|\boldsymbol{\mu}_2|^2)^{7/6} \qquad (12)$$

where C_1 and C_2 are constants. This expression follows directly from eq 10 with the assumption that all of the parameters other than the dipole moment of the solvent molecule are fixed; a simpler, approximate form was used in the previous work on BChl solutions.[22] Figure 10 plots the mean frequency of the rapidly damped components observed in the ZnTMPyP solutions as a function of the gas-phase dipole moment of the solvent. The mode frequency increases as the dipole moment increases in a manner that is consistent with the form of eq 12. The fit of the mode frequencies to eq 12 extrapolates to a mode frequency near 70 cm^{-1} in the nonpolar limit. As anticipated in the Introduction, this y intercept value is significantly lower than the value of ∼100 cm^{-1} observed in BChl solution. ZnTMPyP's four-fold symmetry results in a dipole moment of zero in the plane of the porphyrin; the out-of-plane doming of the Zn^{II} ion due to the axial coordination of a solvent ligand results in a small dipole-moment component orthogonal to the plane of the porphyrin (0.66 D, as obtained from the B3LYP 6−31G electronic structure calculation for the methanol complex, see Figure 1). The dipole moment of BChl is significantly larger (3.6 D,[68] so the $\alpha_2|\boldsymbol{\mu}_1|^2$ induction term in eqs 9 and 10 that contributes to the y intercept constant C_1 in eq 12 is more than 25 times smaller for ZnTMPyP since this term scales as the square of the dipole moment. The remaining term in eqs 9 and 10 that contributes to the y intercept term of eq 12 is the London-dispersion term, $b\alpha_1\alpha_2$. Thus, a great deal of the residual 70

cm^{-1} of the *y* intercept value obtained for ZnTMPyP is due to the London-dispersion term. This conclusion is consistent with the general observation that the dipole−dipole and London−dispersion terms in the intermolecular potential are perhaps 10 times larger than either of the induction terms.[63−66]

Some of the molecular details of the interaction between ZnTMPyP and the surrounding solvent are suggested by deviations from the fitted curve shown in Figure 10 and by the dependence of the resonance Raman activity for the intermolecular mode on the solvent. The reduction of eq 10 to eq 12 requires that the polarizability α_2 for the solvent molecule is constant as the dipole moment $\boldsymbol{\mu}_2$ varies. The dispersion of the points for the solvents DMSO, CH_3CN, and DMF from the fitted curve in Figure 10 suggests a possible contribution of the solvent polarizability in the strength of the intermolecular interaction with the ZnTMPyP solute. These solvents have similar dipole moments, yet the mean frequency of the intermolecular mode varies in them over the $95-125$ cm^{-1} range, a span of about one-fifth of the mean value. The increase of the mean frequency from that observed in methanol ($\alpha_2 = 3.29$ $Å^3$ [67]), 79 cm^{-1}, to that for acetonitrile ($\alpha_2 = 4.4$ $Å^3$ [67]), 106 cm^{-1}, depends mostly on the induction term $\alpha_1|\boldsymbol{\mu}_2|^2$ since the dipole−dipole term $c|\boldsymbol{\mu}_1|^2|\boldsymbol{\mu}_2|^2$ is relatively small owing to the small dipole moment of ZnTMPyP. The induction term is relatively large in porphyrin and BChl solutions because of the large polarizabilities (α_1) of these solutes. The difference between the mean frequency observed in acetonitrile and that observed in DMSO ($\alpha_2 = 8.87$ $Å^3$ [69]), however, probably arises largely from the enhanced polarizability of the sulfonyl group over that of the carbonyl. Further, the decreased mean frequency in DMF ($\alpha_2 = 7.81$ $Å^3$ [67]) has to be attributed to a specific solvent effect that decreases the strength of the intermolecular interaction given that the polarizability of DMF is almost as large as that of DMSO.

The solvent dependence of the amplitude of the rapidly damped modulation components (see Table 2) suggests that the resonance Raman intensity enhancement for the intermolecular mode partly depends on the covalency of the interaction, the degree to which the π-electron density of the solute chromophore is mixed with that of the clustered solvent molecule. The use of a van der Waals potential to follow trends in the mode frequency invokes a purely electrostatic picture, of course, but some involvement of covalency is suggested by the observation that the strongest modulation amplitudes occur in CH_3CN and DMSO, which feature cyanide/nitrile and sulfonyl groups, respectively. This observation follows the same trend observed with *Q*-band excitation of polar solutions of BChl; the amplitude of the intermolecular vibrational coherence was strongest by far in pyridine solution.[22] As mentioned above, DMF seems to be an outlier; the intermolecular modes in DMF and CH_3OH have comparable amplitudes even though the former contains delocalized π-electron density over the amide group. It follows that both the Albrecht A- and the B-terms[70,71] contribute to the resonance Raman intensity. The A-term would primarily include effects from the change of shape and extent of the π-electron density that yield a gradient in the excited-state potential-energy surface in the Franck−Condon region, whereas the B-term would include couplings of the excited-state to nearby states. The part of the A-term enhancement that arises from the redistribution of π-electron density in ZnTMPyP's excited state (see Figure 1) is likely to be small given that the intermolecular modes are easily observed in BChl, which lacks a comparable ground-to-excited-state displacement of electron density.

5. Conclusions

The results discussed in this paper support the hypothesis that intermolecular modes between porphyrin or chlorophyll macrocycles and clustered molecules in the first shell of solvent contribute the most intense components to the low-frequency $(0-300$ $cm^{-1})$ vibrational coherence in polar media. The corresponding mode frequencies fall in the right range to account for the modes that dominate the Marcus reorganization energy for electron-transfer reactions in photosynthetic reaction centers. In comparison to the intermolecular modes, the intramolecular modes from the porphyrin or chlorophyll macrocycle account for features in the vibrational coherence that are at least an order of magnitude weaker. Further, an analysis of the electronic structure of ZnTMPyP suggests that there should be a significant ground-to-excited-state change in the mode frequency and stabilization of the intermolecular modes owing to the change in shape of the π-electron density. The contribution of ion−dipole and ion−induced-dipole terms to the intermolecular potential in the excited-state of ZnTMPyP should result in a significantly higher intermolecular mode frequency. These projections suggest an important role for intermolecular modes between the prosthetic groups and their first-solvation-shell surroundings in the stabilization of the charged intermediate and product species that occur in proteins during redox catalysis.

References and Notes

(1) Bixon, M.; Jortner, J. Coupling of protein modes to electron transfer in bacterial photosynthesis. *J. Phys. Chem.* **1986**, *90*, 3795–3800.

(2) Fleming, G. R.; Martin, J.-L.; Breton, J. Rates of primary electron transfer in photosynthetic reaction centers and their mechanistic implications. *Nature* **1988**, *333*, 190–192.

(3) Bixon, M.; Jortner, J. Activationless and pseudoactivationless primary electron transfer in photosynthetic bacterial reaction centers. *Chem. Phys. Lett.* **1989**, *159*, 17–20.

(4) Vos, M. H.; Lambry, J. C.; Robles, S. J.; Youvan, D. C.; Breton, J.; Martin, J. L. Direct observation of vibrational coherence in bacterial reaction centers using femtosecond absorption spectroscopy. *Proc. Natl. Acad. Sci. U.S.A.* **1991**, *88*, 8885–8889.

(5) Vos, M. H.; Lambry, J. C.; Robles, S. J.; Youvan, D. C.; Breton, J.; Martin, J. L. Femtosecond spectral evolution of the excited state of bacterial reaction centers at 10 K. *Proc. Natl. Acad. Sci. U.S.A.* **1992**, *89*, 613–617.

(6) Vos, M. H.; Rappaport, F.; Lambry, J.-C.; Breton, J.; Martin, J.-L. Visualization of the coherent nuclear motion in a membrane protein by femtosecond spectroscopy. *Nature* **1993**, *363*, 320–325.

(7) Vos, M. H.; Jones, M. R.; Hunter, C. N.; Breton, J.; Lambry, J.-C.; Martin, J.-L. Coherent dynamics during the primary electron-transfer reaction in membrane-bound reaction centers of *Rhodobacter sphaeroides*. *Biochemistry* **1994**, *33*, 6750–6757.

(8) Vos, M. H.; Jones, M. R.; Hunter, C. N.; Breton, J.; Martin, J.-L. Coherent nuclear dynamics at room temperature in bacterial reaction centers. *Proc. Nat. Acad. Sci. U.S.A.* **1994**, *91*, 12701–12705.

(9) Vos, M. H.; Jones, M. R.; Breton, J.; Lambry, J.-C.; Martin, J.-L. Vibrational dephasing of long- and short-lived primary donor states in mutant reaction centers of Rhodobacter sphaeroides. *Biochemistry* **1996**, *35*, 2687–2692.

(10) Vos, M. H.; Jones, M. R.; Martin, J. L. Vibrational coherence in bacterial reaction centers: spectroscopic characterisation of motions active during primary electron transfer. *Chem. Phys.* **1998**, *233*, 179–190.

(11) Rischel, C.; Spiedel, D.; Ridge, J. P.; Jones, M. R.; Breton, J.; Lambry, J.-C.; Martin, J.-L.; Vos, M. H. Low frequency vibrational modes in proteins: changes induced by point-mutations in the protein-cofactor matrix of bacterial reaction centers. *Proc. Natl. Acad. Sci. U.S.A.* **1998**, *95*, 12306–12311.

(12) Vos, M. H.; Martin, J.-L. Femtosecond processes in proteins. *Biochim. Biophys. Acta* **1999**, *1411*, 1–20.

(13) Stanley, R. J.; Boxer, S. G. Oscillations in the spontaneous fluorescence from photosynthetic reaction centers. *J. Phys. Chem.* **1995**, *99*, 859–863.

(14) Vos, M. H.; Rischel, C.; Jones, M. R.; Martin, J. L. Electrochromic detection of a coherent component in the formation of the charge pair $P^+H_L^-$ in bacterial reaction centers. *Biochemistry* **2000**, *39*, 8353–8361.

(15) Yakovlev, A.; Shkuropatov, A.; Shuvalov, V. Nuclear wavepacket motion producing a reversible charge separation in bacterial reaction centers. *FEBS Lett.* **2000**, *466*, 209–212.

(16) Yakovlev, A.; Shkuropatov, A.; Shuvalov, V. Nuclear wavepacket motion between P* and $P^+B_A^-$ potential surfaces with a subsequent electron transfer to H_A in bacterial reaction centers. 1. Room temperature. *Biochemistry* **2002**, *41*, 2667–2674.

(17) Yakovlev, A.; Shkuropatov, A.; Shuvalov, V. Nuclear wave packet motion between P* and $P^+B_A^-$ potential surfaces with a subsequent electron transfer to HA in bacterial reaction centers at 90 K. Electron transfer pathway. *Biochemistry* **2002**, *41*, 14019–14027.

(18) Shuvalov, V.; Yakovlev, A. Coupling of nuclear wavepacket motion and charge separation in bacterial reaction centers. *FEBS Lett.* **2003**, *540*, 26–34.

(19) Spörlein, S.; Zinth, W.; Wachtveitl, J. Vibrational coherence in photosynthetic reaction centers observed in the bacteriochlorophyll anion band. *J. Phys. Chem. B* **1998**, *102*, 7492–7496.

(20) Huppmann, P.; Spörlein, S.; Bibikova, M.; Oesterhelt, D.; Wachtveitl, J.; Zinth, W. Electron transfer in reaction centers of *Blastochloris viridis*: photosynthetic reactions approximating the adiabatic regime. *J. Phys. Chem. A* **2003**, *107*, 8302–8309.

(21) Shelly, K. R.; Carson, E. A.; Beck, W. F. Vibrational coherence from the dipyridine complex of bacteriochlorophyll *a*: intramolecular modes in the $10-220 \ cm^{-1}$ regime, intermolecular solvent modes, and relevance to photosynthesis. *J. Am. Chem. Soc.* **2003**, *125*, 11810–11811.

(22) Shelly, K. R.; Golovich, E. C.; Beck, W. F. Intermolecular vibrational coherence in bacteriochlorophyll *a* with clustered polar solvent molecules. *J. Phys. Chem. B* **2006**, *110*, 20586–20595.

(23) Shelly, K. R.; Golovich, E. C.; Beck, W. F. Intermolecular vibrational coherence in the purple-bacterial light-harvesting proteins B777 and B820 from *Rhodospirillum rubrum*. *J. Phys. Chem. B* **2008**, *112*, 1299–1307.

(24) Palaniappan, V.; Aldema, M. A.; Frank, H. A.; Bocian, D. F. Q_y-excitation resonance Raman scattering from the special pair in *Rhodobacter sphaeroides* reaction centers. Implications for primary charge separation. *Biochemistry* **1992**, *31*, 11050–11058.

(25) Czarnecki, K.; Diers, J. R.; Chynwat, V.; Erickson, J. P.; Frank, H. A.; Bocian, D. F. Characterization of the strongly coupled, low-frequency vibrational modes of the special pair of photosynthetic reaction centers via isotopic labeling of the cofactors. *J. Am. Chem. Soc.* **1997**, *119*, 415–426.

(26) Walsh, A. M.; Loring, R. F. Theory of resonant and nonresonant impulsive stimulated raman scattering. *Chem. Phys. Lett.* **1989**, *160*, 299–304.

(27) Pollard, W. T.; Fragnito, H. L.; Bigot, J.-Y.; Shank, C. V.; Mathies, R. A. Quantum-mechanical theory for 6 fs dynamic absorption spectroscopy and its application to nile blue. *Chem. Phys. Lett.* **1990**, *168*, 239–245.

(28) Pollard, W. T.; Lee, S.-Y.; Mathies, R. A. Wave packet theory of dynamic absorption spectra in femtosecond pump-probe experiments. *J. Chem. Phys.* **1990**, *92*, 4012–4029.

(29) Dexheimer, S. L.; Wang, Q.; Peteanu, L. A.; Pollard, W. T.; Mathies, R. A.; Shank, C. V. Femtosecond impulsive excitation of nonstationary vibrational states in bacteriorhodopsin. *Chem. Phys. Lett.* **1992**, *188*, 61–66.

(30) Pollard, W. T.; Dexheimer, S. L.; Wang, Q.; Peteanu, L. A.; Shank, C. V.; Mathies, R. A. Theory of dynamic absorption spectroscopy of nonstationary states. 4. Application to 12-fs resonant impulsive Raman spectroscopy of bacteriorhodopsin. *J. Phys. Chem.* **1992**, *96*, 6147–6158.

(31) Pollard, W. T.; Mathies, R. A. Analysis of femtosecond dynamic absorption spectra of nonstationary states. *Annu. Rev. Phys. Chem.* **1992**, *43*, 497–523.

(32) Frisch, M. J.; Trucks, G. W.; Schlegel, H. B.; Scuseria, G. E.; Robb, M. A.; Cheeseman, J. R.; Montgomery, J. A., Jr.; Vreven, T.; Kudin, K. N.; Burant, J. C.; Millam, J. M.; Iyengar, S. S.; Tomasi, J.; Barone, V.; Mennucci, B.; Cossi, M.; Scalmani, G.; Rega, N.; Petersson, G. A.; Nakatsuji, H.; Hada, M.; Ehara, M.; Toyota, K.; Fukuda, R.; Hasegawa, J.; Ishida, M.; Nakajima, T.; Honda, Y.; Kitao, O.; Nakai, H.; Klene, M.; Li, X.; Knox, J. E.; Hratchian, H. P.; Cross, J. B.; Bakken, V.; Adamo, C.; Jaramillo, J.; Gomperts, R.; Stratmann, R. E.; Yazyev, O.; Austin, A. J.; Cammi, R.; Pomelli, C.; Ochterski, J. W.; Ayala, P. Y.; Morokuma, K.; Voth, G. A.; Salvador, P.; Dannenberg, J. J.; Zakrzewski, V. G.; Dapprich, S.; Daniels, A. D.; Strain, M. C.; Farkas, O.; Malick, D. K.; Rabuck, A. D.; Raghavachari, K.; Foresman, J. B.; Ortiz, J. V.; Cui, Q.; Baboul, A. G.; Clifford, S.; Cioslowski, J.; Stefanov, B. B.; Liu, G.; Liashenko, A.; Piskorz, P.; Komaromi, I.; Martin, R. L.; Fox, D. J.; Keith, T.; Al-Laham, M. A.; Peng, C. Y.; Nanayakkara, A.; Challacombe, M.; Gill, P. M. W.; Johnson, B.; Chen, W.; Wong, M. W.; Gonzalez, C.; Pople, J. A. *Gaussian 03, Revision D.01*; Gaussian, Inc.: Wallingford, CT, 2004.

(33) Lakowicz, J. R. *Principles of Fluorescence Spectroscopy*; Second ed.; Kluwer Academic/Plenum Publishers: New York, 1999.

(34) Fragnito, H. L.; Bigot, J.-Y.; Becker, P. C.; Shank, C. V. Evolution of the vibronic absorption spectrum in a molecule following impulsive excitation with a 6-fs optical pulse. *Chem. Phys. Lett.* **1989**, *160*, 101–104.

(35) Schoenlein, R. W.; Peteanu, L. A.; Mathies, R. A.; Shank, C. V. The first step in vision: femtosecond isomerization of rhodopsin. *Science* **1991**, *254*, 412–415.

(36) Wang, Q.; Schoenlein, R. W.; Peteanu, L. A.; Mathies, R. A.; Shank, C. V. Vibrationally coherent photochemistry in the femtosecond primary event of vision. *Science* **1994**, *266*, 422–424.

(37) Zhu, L.; Li, P.; Huang, M.; Sage, J. T.; Champion, P. M. Real time observation of low frequency heme protein vibrations using femtosecond coherence spectroscopy. *Phys. Rev. Lett.* **1994**, *72*, 301–304.

(38) Wang, W.; Demidov, A.; Ye, X.; Christian, J. F.; Sjodin, T.; Champion, P. M. Application of femtosecond coherence spectroscopy to the observation of nuclear motions in heme proteins and transparent solutions. *J. Raman Spectrosc.* **2000**, *31*, 99–105.

(39) Rosca, F.; Ionascu, D.; Kumar, A. T. N.; Demidov, A. A.; Champion, P. M. Femtosecond coherence spectroscopy using spectrally selective differential photodetection. *Chem. Phys. Lett.* **2001**, *337*, 107–116.

(40) Cantor, C. R.; Schimmel, P. R. , *Biophysical Chemistry. Part II: Techniques for the Study of Biological Structure and Function*; W. H. Freeman and Company: San Francisco, 1980.

(41) McHale, J. L. *Molecular Spectroscopy*; Prentice Hall: Upper Saddle River, NJ, 1999.

(42) Cong, P.; Deuhl, H. P.; Simon, J. D. Using optical coherence to measure the ultrafast electronic dephasing of large molecules in room-temperature liquids. *Chem. Phys. Lett.* **1993**, *211*, 367–373.

(43) Joo, T.; Jia, Y.; Yu, J.-Y.; Lang, M. J.; Fleming, G. R. Third-order nonlinear time domain probes of solvation dynamics. *J. Chem. Phys.* **1996**, *104*, 6089–6108.

(44) Xu, Q.-H.; Ma, Y.-Z.; Stiopkin, I. V.; Fleming, G. R. Wavelength-dependent resonant homodyne and heterodyne transient grating spectroscopy with a diffractive optics method: Solvent effect on the third-order signal. *J. Chem. Phys.* **2002**, *116*, 9333–9340.

(45) Stratt, R. M. The instantaneous normal modes of liquids. *Acc. Chem. Res.* **1995**, *28*, 201–207.

(46) Stratt, R. M.; Maroncelli, M. Nonreactive dynamics in solution: the emerging molecular view of solvation dynamics and vibrational relaxation. *J. Phys. Chem.* **1996**, *100*, 12981–12996.

(47) Siano, D. B.; Metzler, D. E. Band shapes of the electronic spectra of complex molecules. *J. Chem. Phys.* **1969**, *51*, 1856–1861.

(48) Vanden Bout, D.; Berg, M. Ultrafast Raman echo experiments in liquids. *J. Raman Spectrosc.* **1995**, *26*, 503–511.

(49) Berg, M.; Vanden Bout, D. A. Ultrafast Raman echo measurements of vibrational dephasing and the nature of solvent−solute interactions. *Acc. Chem. Res.* **1997**, *30*, 65–71.

(50) Carson, E. A.; Diffey, W. M.; Shelly, K. R.; Lampa-Pastirk, S.; Dillman, K. L.; Schleicher, J. M.; Beck, W. F. Dynamic-absorption spectral contours: Vibrational phase-dependent resolution of low-frequency coherent wave-packet motion of IR144 on the ground and excited $\pi{\rightarrow}\pi^*$ surfaces. *J. Phys. Chem. A* **2004**, *108*, 1489–1500.

(51) Yu, H.-Z.; Baskin, J. S.; Zewail, A. H. Ultrafast dynamics of porphyrins in the condensed phase: II. Zinc tetraphenylporphyrin. *J. Phys. Chem. A* **2002**, *106*, 9845–9854.

(52) Yoon, M.-C.; Jeong, D. H.; Cho, S.; Kim, D.; Rhee, H.; Joo, T. Ultrafast transient dynamics of Zn(II) porphyrins: observation of vibrational coherence by controlling chirp of femtosecond pulses. *J. Chem. Phys.* **2003**, *118*, 164–171.

(53) Enescu, M.; Steenkeste, K.; Tfibel, F.; Fontaine-Aupart, M.-P. Femtosecond relaxation processes from upper excited states of tetrakis(N-methyl-4-pyridyl)porphyrins studied by transient absorption spectroscopy. *Phys. Chem. Chem. Phys.* **2002**, *4*, 6092–6099.

(54) Jean, J. M.; Fleming, G. R. Competition between energy and phase relaxation in electronic curve crossing processes. *J. Chem. Phys.* **1995**, *103*, 2092–2101.

(55) Franzen, S.; Fritsch, K.; Brewer, S. H. Experimental observation of anharmonic coupling of the heme-doming and iron-ligand out-of-plane vibrational modes confirmed by density functional theory. *J. Phys. Chem. B* **2002**, *106*, 11641–11646.

(56) Morikis, D.; Li, P.; Bangcharoenpaurpong, O.; Sage, J. T.; Champion, P. M. Resonance Raman scattering as a probe of electron−nuclear coupling: applications to heme proteins. *J. Phys. Chem.* **1991**, *95*, 3391–3398.

(57) Ladanyi, B. M.; Stratt, R. M. Short-time dynamics of solvation: linear solvation theory for polar solvents. *J. Phys. Chem.* **1995**, *99*, 2502–2511.

Vibrational Coherence in Polar Solutions

J. Phys. Chem. B, Vol. 113, No. 17, 2009 **6139**

(58) Wilson Jr., E. B.; Decius, J. C.; Cross, P. C. *Molecular Vibrations: The Theory of Infrared and Raman Vibrational Spectra*; McGraw-Hill: New York, 1955.

(59) Garg, S. K.; Smyth, C. P. Microwave absorption and molecular structures in liquids. LXII. The three dielectric dispersion regions of the normal primary alcohols. *J. Phys. Chem.* **1965**, *69*, 1294–1301.

(60) Jorgensen, W. L. Structure and properties of liquid methanol. *J. Am. Chem. Soc.* **1980**, *102*, 543–549.

(61) Bertolini, D.; Cassettari, M.; Salvetti, G. The dielectric properties of alcohols−water solutions. I. The alcohol rich region. *J. Chem. Phys.* **1983**, *78*, 365–372.

(62) Sumi, H.; Marcus, R. A. Dielectric relaxation and intramolecular electron transfers. *J. Chem. Phys.* **1986**, *84*, 4272–4276.

(63) London, F. The general theory of molecular forces. *Trans. Faraday Soc.* **1937**, *33*, 8–26.

(64) Margenau, H. Van der Waals forces. *Rev. Mod. Phys.* **1939**, *11*, 1–35.

(65) Kauzmann, W. *Quantum Chemistry: An Introduction*; Academic Press, New York, 1957.

(66) Berry, R. S.; Rice, S. A.; Ross, J. *Physical Chemistry*; Second ed.; Oxford University Press: New York, 2000.

(67) Lide, D. R., Ed. *CRC Handbook of Chemistry and Physics*; 87th edition ed.; CRC Press, Inc.: Boca Raton, FL, 2006.

(68) He, Z.; Sundström, V.; Pullerits, T. Excited states of carotenoid in LH2: an ab initio study. *Chem. Phys. Lett.* **2001**, *334*, 159–167.

(69) Jin, R.-H.; Aoki, S.; Shima, K. Phosphoniumyl cationic porphyrins: self-aggregation origin from $\pi-\pi$ and cation$-\pi$ interactions. *J. Chem. Soc., Faraday Trans.* **1997**, *93*, 3945–3953.

(70) Albrecht, A. C. "Forbidden" character in allowed electronic transitions. *J. Chem. Phys.* **1960**, *33*, 156–169.

(71) Tang, J.; Albrecht, A. C. Developments in the theories of vibrational Raman intensities. In *Raman Spectroscopy: Theory and Practice*; Szymanski, H. A., Ed.; Plenum: New York, 1970; Vol. 2, pp 33−68.